Supplemental Document

optica

Polarization-sensitive optical diffraction tomography: supplement

AMIRHOSSEIN SABA,* JOOWON LIM, AHMED B. AYOUB, ELIZABETH E. ANTOINE, AND DEMETRI PSALTIS

Optics Laboratory, École polytechnique fédérale de Lausanne, CH-1015, Lausanne, Switzerland
**Corresponding author: amirhossein.sabashirvan@epfl.ch*

Supplement DOI: https://doi.org/10.6084/m9.figshare.13718146

Parent Article DOI: https://doi.org/10.1364/OPTICA.415343

Polarization-sensitive optical diffraction tomography: supplementary document

1. LIGHT PROPAGATION IN ANISOTROPIC INHOMOGENEOUS MEDIA AND VECTORIAL INVERSE SCATTERING

Here, we discuss the propagation of light and scattering problem for a weak anisotropic scatterer placed in a homogeneous and isotropic background medium. Starting from Maxwell's equations for a monochromatic wave,

$$\nabla \times \vec{E} = j\omega\vec{B} \tag{S1a}$$

$$\nabla \times \vec{B} = -j\omega/c^2\bar{\bar{\varepsilon}}_r\vec{E} \tag{S1b}$$

where, $\bar{\bar{\varepsilon}}_r$ is the relative permittivity tensor, ω is the temporal frequency, and c is the speed of light in vacuum, we can get the following equation,

$$\nabla \times \nabla \times \vec{E} = -\nabla^2\vec{E} + \nabla\nabla \cdot \vec{E} = \omega^2/c^2\bar{\bar{\varepsilon}}_r\vec{E} \tag{S2}$$

We can define the refractive index tensor of the birefringent sample as,

$$\bar{\bar{\varepsilon}}_r = \left(n_0\mathbb{1} + \overline{\overline{\delta n}}\right)^2 \approx n_0^2\mathbb{1} + 2n_0\overline{\overline{\delta n}} = n_0^2\mathbb{1} + \overline{\overline{\delta\varepsilon}} \tag{S3}$$

where, n_0 is the refractive index of the isotropic background medium, and $\overline{\overline{\delta n}}$ and $\overline{\overline{\delta\varepsilon}}$ are the refractive index and permittivity tensors of the anisotropic scatterer relative to the background. $\mathbb{1}$ is the identity matrix. Diagonalization of the refractive index tensor we defined in Eq. S3 yields the phase velocity of the polarization eigenstates. The term of $\nabla\nabla \cdot \vec{E}$ can lead to polarization coupling even in the absence of birefringence, i.e. for a sample with scalar permittivity. This term can be neglected if the scale of the variation of the permittivity (or the envelope of the field) is much larger than the wavelength (the slowly varying envelope approximation), $\lambda \ll \xi(\delta\varepsilon)$ [1] [1] , which is equivalent to the paraxiality [2]. We assume that the only reason for polarization coupling is the birefringence of the sample since the sample varies slowly with respect to the wavelength. The total field vector, $\vec{E}$, can be represented as the summation of the incident, $\vec{E}^i$, and scattered, $\vec{E}^s$, field vectors. By considering the fact that $\left(\nabla^2 + k_0^2n_0^2\right)\vec{E}^i = 0$, we have,

$$\left(\nabla^2 + k_0^2n_0^2\right)\vec{E}^s = -k_0^2\overline{\overline{\delta\varepsilon}}\vec{E} \tag{S4}$$

k_0 is the light wave-vector in the free-space. The right hand side of this equation is a vector that functions as a scattering source, and we look for the solution of vector $\vec{E}^s$ that satisfies Eq. S4. The left hand side of this equation is related to the background medium, n_0 which is isotropic and homogenous. This makes each component of these vectors (left and right side) uncoupled from each other. So, the Green's function of this equation can be represented by a diagonal tensor with same components for each polarization,

$$\overline{\overline{G}} = \begin{pmatrix} g(r,r') & 0 & 0 \\ 0 & g(r,r') & 0 \\ 0 & 0 & g(r,r') \end{pmatrix} \tag{S5}$$

[1] $\xi(\delta\varepsilon)$ is the correlation length of the inhomogeneity of the sample, which can be defined as $\langle \delta\varepsilon(r) | \delta\varepsilon(r') \rangle \approx e^{-(r-r')/\xi}$.

in which, $g(r,r') = e^{jk_0 n_0 (r-r')}/|r-r'|$, same as the scalar case. Now, we assume the first-order Born approximation, and replace the field vector in the right hand side of Eq. S4 with the input unperturbed beam. Defining the scattering potential tensor as $\overline{\overline{V}} = k_0^2 \overline{\overline{\delta\varepsilon}}/4\pi$, we can represent the scattered field vector as,

$$\vec{E}^s(r) = \int \overline{\overline{G}}(r,r') \times \overline{\overline{V}}(r') \times \vec{E}^{illum}(r')\, d^3r' \tag{S6}$$

There is an important point regarding Eq. S6. In Eq. (15) of [3], the scattered field under the Born approximation is derived as,

$$\vec{E}^s(|r|\,\hat{u}) = \int \overline{\overline{G}}(r,r') \times \overline{\overline{V}}(r') \times \left(\vec{E}^{illum}(r') - \hat{u}\cdot\vec{E}^{illum}(r')\right) d^3r' \tag{S7}$$

$\hat{u}$ is the unit vector along the scattered field component. Unlike Eq. S6, Eq. S7 has the $\hat{u}\cdot\vec{E}^{illum}$ term. It can be followed in [3] that this term is coming from $\nabla\nabla\cdot\vec{E}$ in the vectorial Helmholtz equation which we neglected. In the topic of paraxiality, we can say that the scattered field has the spatial frequency components that are very close to the incident illumination, $\vec{k}_i$, and as a result, we will have $\hat{u}\cdot\vec{E}^{illum} \approx 0$ which will lead to the same equation as ours. This shows the equivalence of the slowly varying approximation, paraxiality, and the approximation that the light does not depolarize due to the inhomogeneity of the sample. It should be noted that in the scalar case, the relationship between the scattered field and the scattering potential becomes linear, under the Born approximation. However, if we do not neglect the $\nabla\nabla\cdot\vec{E}$ term, due to the presence of the spatial frequency component of the scattered field, $\hat{u}$, on the right side of Eq. S7, the relationship remains nonlinear even under the Born approximation. This is the reason why we actually neglect this term, which is valid for slowly-varying samples.

In the general case, the scattering potential tensor in Eq. S6 as well as the refractive index tensor are 3×3 tensors. However, the polarization state of the illumination beam $\vec{E}^{illum}$ should be perpendicular to its wave-vector, and as a result, can only have two *independent* states. Lets us consider two separate experiments with two different and independent polarization states for E^{illum}. We can put these two experiments in the same framework by representing the incident field in two different columns of a 3×2 matrix. We assume that the measured fields are in XY coordinate system:

$$\begin{pmatrix} E^s_{x1}(r) & E^s_{x2}(r) \\ E^s_{y1}(r) & E^s_{y2}(r) \\ E^s_{z1}(r) & E^s_{z2}(r) \end{pmatrix} = \int \overline{\overline{G}}(r,r') \times \overline{\overline{V}}(r') \times \begin{pmatrix} E^{illum}_{x1}(r') & E^{illum}_{x2}(r') \\ E^{illum}_{y1}(r') & E^{illum}_{y2}(r') \\ E^{illum}_{z1}(r') & E^{illum}_{z2}(r') \end{pmatrix} d^3r' \tag{S8}$$

By assuming a plane wave illumination, $\vec{E}^{illum}(r') = \tilde{E}^{illum} e^{j\vec{k}_i\cdot r'}$ ($\tilde{E}^{illum}$ is the illumination field amplitude, and $\vec{k}_i$ is its wave-vetor), Eq. S8 can be written as:

$$\begin{pmatrix} E^s_{x1}(r) & E^s_{x2}(r) \\ E^s_{y1}(r) & E^s_{y2}(r) \\ E^s_{z1}(r) & E^s_{z2}(r) \end{pmatrix} = \left[\int \overline{\overline{G}}(r,r') \times \overline{\overline{V}}(r') e^{j\vec{k_i}\cdot r'} d^3r'\right] \times \begin{pmatrix} \tilde{E}^{illum}_{x1} & \tilde{E}^{illum}_{x2} \\ \tilde{E}^{illum}_{y1} & \tilde{E}^{illum}_{y2} \\ \tilde{E}^{illum}_{z1} & \tilde{E}^{illum}_{z2} \end{pmatrix} \tag{S9}$$

It can be seen from Eq. S9 that all the 9 components of the 3×3 scattering potential tensor cannot be retrieved using only two independent input polarization states. We can approximate this equation with a 2×2 representation of the fields and the scattering potential tensors,

$$\begin{pmatrix} E^s_{x1}(r) & E^s_{x2}(r) \\ E^s_{y1}(r) & E^s_{y2}(r) \end{pmatrix} \approx \left[\int \overline{\overline{G}}(r,r') \times \overline{\overline{V}}_{2\times2}(r') e^{j\vec{k_i}\cdot r'} d^3r'\right] \times \begin{pmatrix} \tilde{E}^{illum}_{x1} & \tilde{E}^{illum}_{x2} \\ \tilde{E}^{illum}_{y1} & \tilde{E}^{illum}_{y2} \end{pmatrix} \tag{S10}$$

$\overline{\overline{V}}_{2\times2}$ is the 2×2 block matrix of the full scattering potential tensor whose definition can be clarified as,

$$\overline{\overline{V}} = \begin{pmatrix} \overline{\overline{V}}_{2\times2} & \begin{matrix} V_{xz} \\ V_{yz} \end{matrix} \\ \begin{matrix} V_{zx} & V_{zy} \end{matrix} & V_{zz} \end{pmatrix} \tag{S11}$$

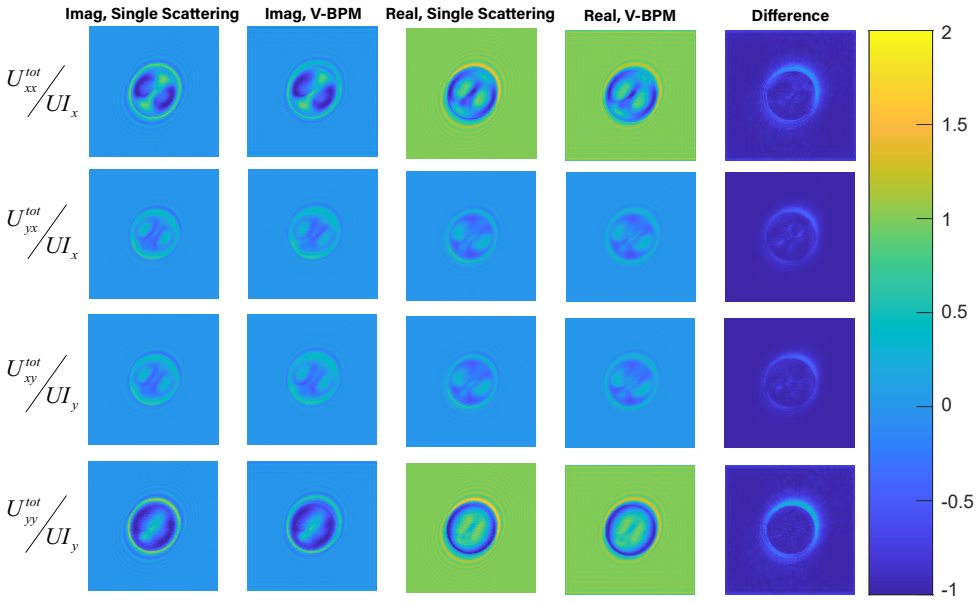

Fig. S1. Comparison of the scattered vectorial fields for the birefringent digital phantom based on the vectorial single scattering and V-BPM. Four rows represent the components of the Jones matrix. First and second columns show the imaginary part of Jones components based on the single scattering and V-BPM model, respectively. Third and fourth columns show the real parts of them, and the last column shows the absolute value of the difference between the single scattering model and V-BPM.

From now, the 2×2 scattering potential tensor is refereed as $\overline{\overline{V}}$ and we drop the 2×2 index. More details about this approximation and accuracy of that is further discussed in section 3 of this document.

Writing Eq. S10 in the Fourier domain and using the Fourier diffraction theorem [4], we arrive at the vectorial version of the Wolf transform as follows:

$$\overline{\overline{V}}(k_x - k_x^{in}, k_y - k_y^{in}, k_z - k_z^{in}) = \frac{k_z}{2\pi j}\mathcal{F}_{2D}\left\{\begin{pmatrix} E^s_{x1} & E^s_{x2} \\ E^s_{y1} & E^s_{y2} \end{pmatrix}\begin{pmatrix} \tilde{E}^{illum}_{x1} & \tilde{E}^{illum}_{x2} \\ \tilde{E}^{illum}_{y1} & \tilde{E}^{illum}_{y2} \end{pmatrix}^{-1}\right\}(k_x, k_y) \tag{S12}$$

where, $k_z = \sqrt{k^2 - k_x^2 - k_y^2}$, and $\mathcal{F}_{2D}$ is the 2D Fourier transform. This equation maps the 2D Fourier components of the Jones matrix to the 3D Fourier components of the scattering potential tensor. The Fourier transforms should be applied independently for each term of the matrices.

2. VECTORIAL BEAM PROPAGATION METHOD

We start from the vectorial Helmholtz equation:

$$\left(\nabla^2 + k_0^2\overline{\overline{\varepsilon}}_r\cdot\right)\vec{E} = 0 \tag{S13}$$

We can define the complex vector envelope of $\vec{\psi}(r)$ as,

$$\vec{E}(r) = \vec{\psi}(r)e^{jk_0 n_0 z} \tag{S14}$$

By assuming the slowly varying envelope approximation and neglecting $\partial^2/\partial z^2\vec{\psi}(r)$, we can rewrite Eq. S13 as follows,

$$\frac{\partial}{\partial z}\vec{\psi}(r) = \frac{j}{2k}\left(\mathbb{1}\nabla_t^2 + k_0^2\overline{\overline{\varepsilon_r}}\right)\vec{\psi}(r) = \mathcal{M}_1\{\vec{\psi}(r)\} + \mathcal{M}_2\{\vec{\psi}(r)\} \tag{S15}$$

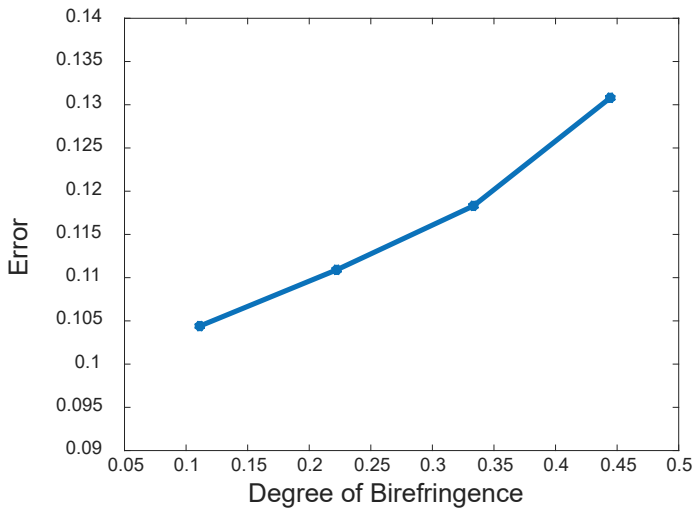

Fig. S2. Error of the single scattering forward model with respect to V-BPM for different digital phantoms as the degree of birefringence increases.

where the diffraction operator, $\mathcal{M}_1$, is a diagonal operator, and $\mathcal{M}_2$ is the phase and amplitude modulation operator. Like the scalar BPM, the solution of this equation can be approximated as,

$$\vec{\psi}\left(x,y,z+dz\right) \approx e^{\mathcal{M}_2 dz} e^{\mathcal{M}_1 dz} \vec{\psi}\left(x,y,z\right) \tag{S16}$$

This approximation comes from the fact that operators $\mathcal{M}_1$ and $\mathcal{M}_2$ do not necessarily commute with each other and as a result we have $e^{(\mathcal{M}_2+\mathcal{M}_1)dz} \neq e^{\mathcal{M}_1 dz} e^{\mathcal{M}_2 dz}$. However, based on the Baker-Campbell-Hausdorff formula [5], we can make this approximation for a small dz. Then, the diffraction operator, $\mathcal{M}_1$, is a diagonal operator which we can be implemented in the Fourier domain:

$$e^{\mathcal{M}_1 dz} \vec{\psi}\left(x,y,z\right) = \mathcal{F}^{-1}\left\{ \mathbb{1} e^{-j\frac{k_x^2+k_y^2}{2k}dz} \times \mathcal{F}\left\{\vec{\psi}\left(x,y,z\right)\right\}\right\} \tag{S17}$$

A more accurate way of implementing the diffraction operator with a nonparaxial version is presented in [6] where we replace the multiplier in Eq. S17 with $exp(-j(k_x^2+k_y^2)/(k+k_z)dz)$. The role of operator $\mathcal{M}_2$ is the phase modulation of the complex vector of $\vec{\psi}\left(x,y,z\right)$, during the propagation through the step, dz, with the refractive index tensor. This is an operator with off-diagonal components which leads to the polarization coupling as light propagates through the birefringence sample. Using Eq. S3, we can write it as,

$$e^{\mathcal{M}_2 dz} \vec{\psi}\left(x,y,z\right) = \text{expm}(jk_0 \overline{\overline{\delta n}}(x,y,z)dz) \times \vec{\psi}\left(x,y,z\right) \tag{S18}$$

operator expm is the matrix exponential. For a matrix, A, the matrix exponential can be defined as,

$$\text{expm}\left(A\right) = \sum_{k=0}^{\infty} \frac{A^k}{k!} \tag{S19}$$

If we diagonalize the matrix $A = UDU^{-1}$, where D is a diagonal matrix with the eigenvalues of A, the exponential of that can be written as $\text{expm}\left(A\right) = Ue^D U^{-1}$. This way, the eigenvalues of the phase modulation matrix in Eq. S18 will be $e^{jk_0\mu_n^1}$ and $e^{jk_0\mu_n^2}$ where $\mu_n^{1,2}$ are the eigenvalues of the refractive index tensor [7].

It should be noted that both amplitudes and phases of each element of the field will change while the overall amplitude of the vector remains unchanged. In [8], it has been shown that we can get more accurate results if we replace dz with $dz/\cos\theta$, owing to the fact that the length of propagation will scale with the illumination angle. Finally, we can write the following equation to summarize V-BPM:

$$\vec{\psi}\left(x,y,z+dz\right) = \text{expm}\left(jk_0 \overline{\overline{\delta n}} dz/\cos\theta\right) \times \mathcal{F}_{2D}^{-1}\left\{ e^{-j\frac{k_x^2+k_y^2}{k+k_z}dz} \times \mathcal{F}_{2D}\left\{\vec{\psi}(x,y,z)\right\}\right\} \tag{S20}$$

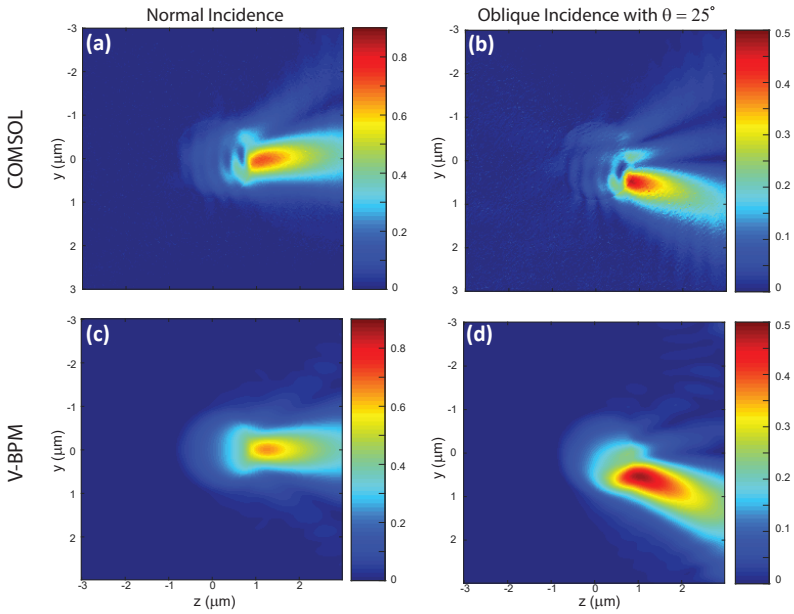

Fig. S3. Verification of V-BPM using FEM: calculated $|E_y|/|E_x^{in}|$ by FEM (COMSOL) for (a) normal incidence and (b) oblique incidence with $\theta = 25^\circ$ and using V-BPM for (c) normal and (d) oblique incidence with $\theta = 25^\circ$.

As the reconstruction method is based on the single scattering model (Rytov approximation), the accuracy of reconstruction is directly related to the validity of the single-scattering approximation. In order to test this validity, we generated synthetic scattered field measurements using V-BPM and compared them with the ones generated using the single scattering model (Eq. S8). For a digital birefringent phantom (same as the one which is shown in section 6), we compare the complex fields achieved after the scattering from the phantom. We show this comparison in Fig. S1. Imaginary and real parts of the complex Jones matrix components are presented. Each row shows one of the 4 components of the Jones matrix, columns show the imaginary and real parts of it, acquired using the single scattering forward model and V-BPM. The last column shows the absolute value of their differences. You can see the pronounced differences around the edges where we have strong scattering. In Fig. S2, we tried 4 different phantoms by increasing the degree of their birefringence (off diagonal refractive index), and we calculated the error between the single scattering model and V-BPM. We can see that the stronger is the birefringence, we have a larger value of error. This is independent from the fact that how much the sample is scattering, while in these 4 phantoms, the strongness of scatterer is relaxed by keeping the diagonal components of the refractive index fixed.

In order to verify the accuracy of our V-BPM, we did a full-wave 3D simulation with finite element method (FEM). This simulation has been done using a commercial FEM solver, COMSOL Multiphysics 5.4. In this simulation, we illuminate a birefringent sphere with a refractive index tensor of

$$\overline{\overline{n}} = n_0 \mathbb{1} + \begin{pmatrix} 0.09 & 0.02 & 0.02 \\ 0.02 & 0.09 & 0.02 \\ 0.02 & 0.02 & 0.09 \end{pmatrix} \tag{S21}$$

which is placed in the background homogeneous medium with refractive index n_0. We study two cases of a normal illumination with input X-polarized light and an oblique illumination with X-polarization state with $\theta = 25^\circ$ in the YZ-plane. Results are presented in Fig. S3. We show the YZ field profiles and compare it with V-BPM. We can see a good agreement between these two methods even for the case of oblique illumination. It should be noted that due to the computational reasons we use a Tetrahedral meshing in the FEM simulation and a rectangular meshing in the V-BPM.

3. APPROXIMATION OF THE 3×3 SCATTERING POTENTIAL TENSOR WITH A 2×2 TENSOR

As discussed in section 1 of this document, the refractive index and the scattering potential tensor are 3×3 tensors in the general case. However, considering Eq. S8, we need *three* independent illumination polarization states to make the illumination field tensor an invertible matrix. We can explain this issue using Jones formalism, in which the Jones matrix of the sample for each illumination angle can be defined as $\vec{E}^t = \vec{E}^s + \vec{E}^{illum} = \bar{\bar{J}}\vec{E}^{illum}$. We can rewrite Eq. S9 using Jones formalism as,

$$\left(\bar{\bar{J}}_{3\times3}(r) - \mathbb{1}_{3\times3}\right) e^{j\vec{k_i}.r} = \left[\int \bar{\bar{G}}\left(r, r'\right) \times \bar{\bar{V}}(r') e^{j\vec{k_i}.r'} d^3r'\right] \tag{S22}$$

Reconstruction of full 3×3 scattering potential tensor is possible using the Fourier diffraction theorem (similar to Eq. S12), if we had the full 3×3 Jones matrix for each illumination angle. However, retrieval of such a Jones matrix is not feasible with 3×2 field tensors that we have in Eq. S8.

In this regard we substitute the 3×3 Jones matrix and scattering potential tensor in Eq. S22 with 2×2 tensors and discuss the justification and validity range of this approximation. Using the Jones formalism, we can write the following matrix representation,

$$\begin{pmatrix} E_{x1}^{out} & E_{x2}^{out} \\ E_{y1}^{out} & E_{y2}^{out} \\ E_{z1}^{out} & E_{z2}^{out} \end{pmatrix} = \begin{pmatrix} J_{xx} & J_{xy} & J_{xz} \\ J_{yx} & J_{yy} & J_{yz} \\ J_{zx} & J_{zy} & J_{zz} \end{pmatrix} \begin{pmatrix} E_{x1}^{illum} & E_{x2}^{illum} \\ E_{y1}^{illum} & E_{y2}^{illum} \\ E_{z1}^{illum} & E_{z2}^{illum} \end{pmatrix} \tag{S23}$$

Clearly, we do not have enough equations to find a 3×3 Jones matrix from these fields. We can rewrite this equation using block-matrices:

$$\begin{pmatrix} \bar{\bar{E}}_{2\times2}^{out} \\ E_{z1}^{out} \quad E_{z2}^{out} \end{pmatrix} = \begin{pmatrix} \bar{\bar{J}}_{2\times2} & \begin{matrix} J_{xz} \\ J_{yz} \end{matrix} \\ \begin{matrix} J_{zx} & J_{zy} \end{matrix} & J_{zz} \end{pmatrix} \begin{pmatrix} \bar{\bar{E}}_{2\times2}^{illum} \\ E_{z1}^{illum} \quad E_{z2}^{illum} \end{pmatrix} \tag{S24}$$

as a result we will have,

$$\bar{\bar{E}}_{2\times2}^{out} = \bar{\bar{J}}_{2\times2} \times \bar{\bar{E}}_{2\times2}^{illum} + \begin{pmatrix} J_{xz}E_{z1}^{illum} & J_{xz}E_{z2}^{illum} \\ J_{yz}E_{z1}^{illum} & J_{yz}E_{z2}^{illum} \end{pmatrix} \tag{S25}$$

Using the rotational matrix which is described in Eq. (5) of the manuscript, we can find the components of E^{illum}. In the case of left-handed and right-handed input polarizations we have $E_{z1}^{illum} = -\sin\theta\cos\left(\pi/4 - \varphi\right)$ and $E_{z2}^{illum} = \sin\theta\cos\left(\pi/4 + \varphi\right)$. So, we will have,

$$\bar{\bar{J}}_{2\times2} = \bar{\bar{E}}_{2\times2}^{out} \times \left(\bar{\bar{E}}_{2\times2}^{illum}\right)^{-1} - \sin\theta \begin{pmatrix} -J_{xz}\cos\left(\pi/4 - \varphi\right) & J_{xz}\cos\left(\pi/4 + \varphi\right) \\ -J_{yz}\cos\left(\pi/4 - \varphi\right) & J_{yz}\cos\left(\pi/4 + \varphi\right) \end{pmatrix} \left(\bar{\bar{E}}_{2\times2}^{illum}\right)^{-1} \tag{S26}$$

The first term of Eq. S26 is what we use in Eq. S12 to reconstruct 2×2 scattering potential. We call it as the approximated Jones matrix, $\bar{\bar{J}}_{2\times2}^{appro}$. On the other hand, we call the Jones matrix including the right term in Eq. S26 as the true Jones matrix, $\bar{\bar{J}}_{2\times2}^{true}$.

We can rewrite Eq. S26 as follows,

$$\bar{\bar{J}}_{2\times2}^{true} = \bar{\bar{J}}_{2\times2}^{appro} - \begin{pmatrix} f_{11}(\theta,\varphi)J_{xz} & f_{12}(\theta,\varphi)J_{xz} \\ f_{21}(\theta,\varphi)J_{yz} & f_{22}(\theta,\varphi)J_{yz} \end{pmatrix} \tag{S27}$$

where $f_{11}(\theta,\varphi)$, $f_{12}(\theta,\varphi)$, $f_{21}(\theta,\varphi)$, and $f_{22}(\theta,\varphi)$ can be found using Eq. Eq. S26 after inversion of $\bar{\bar{E}}_{2\times2}^{illum}$.

We show the values of $f_{11}(\theta,\varphi)$, $f_{12}(\theta,\varphi)$, $f_{21}(\theta,\varphi)$, and $f_{22}(\theta,\varphi)$, in Fig. S4(a) for illuminations with a conical pattern. We can see that the maximum of these values is $\sin\theta$, which relates to the

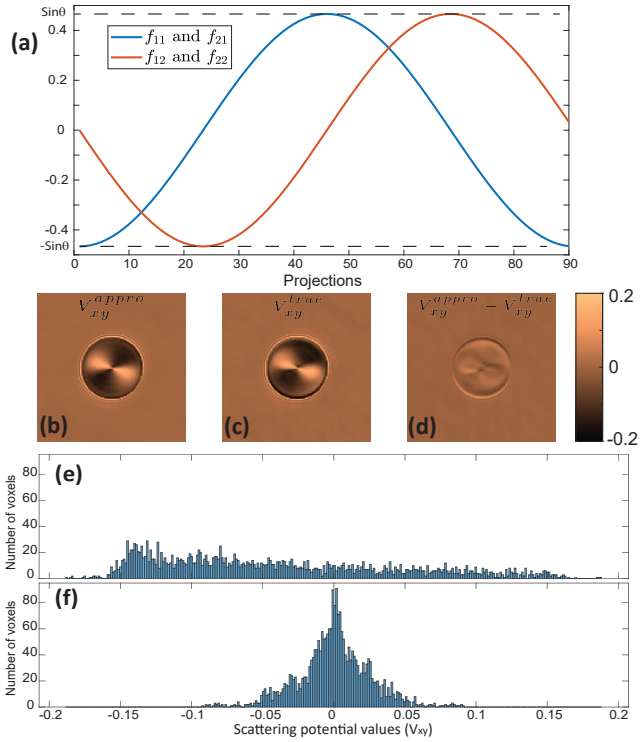

Fig. S4. (a) Values of $f_{11}(\theta,\varphi)$, $f_{12}(\theta,\varphi)$, $f_{21}(\theta,\varphi)$, and $f_{22}(\theta,\varphi)$ for 90 projections with a conical pattern. (b) Calculated V_{xy}^{appro}, (c) V_{xy}^{true}, and (d) their difference regrading Eq. S28. (e) Histogram diagram of the true scattering potential values, and (f) the difference regrading Eq. S28.

NA of the objectives. In our case, $\sin\theta = 0.4$ and the method is more accurate for illumination angles with smaller θ. For many cases like tissues that are placed on a coverslip (in XY-plane), the J_{xz} and J_{yz} terms are negligible as the tissue fibers are in XY-plane. However, even for the cases with J_{xz} and J_{yz} comparable to J_{xy} and J_{yx}, almost 50 % of projections have $f(\theta,\varphi)$ valuse smaller than 0.3.

However, the main reason that this is a good approximation can be justified by applying Fourier diffraction theorem on Eq. S27. Wolf's method is a linear transform, and as a result,

$$\overline{\overline{V}}_{2\times2}^{true}(k_x-k_x^{in},k_y-k_y^{in},k_z-k_z^{in}) = \overline{\overline{V}}_{2\times2}^{appro}(k_x-k_x^{in},k_y-k_y^{in},k_z-k_z^{in}) - \frac{k_z}{2\pi j}\mathcal{F}_{2D}\left\{\begin{pmatrix} f_{11}(\theta,\varphi)J_{xz} & f_{12}(\theta,\varphi)J_{xz} \\ f_{21}(\theta,\varphi)J_{yz} & f_{22}(\theta,\varphi)J_{yz}\end{pmatrix} e^{j\vec{k}_{in}\cdot\vec{r}}\right\}(k_x,k_y) \tag{S28}$$

the second term in Eq. S28 is the 3D tensorial reconstruction which is achieved by applying Wolf's method on 2D components of the tensor. It can be seen in Fig. S6 that Jones matrix components change slightly for different illumination angles, and especially for the case of a thin-transparency, Jones matrix components such as J_{xz} or J_{yz} remain exactly similar for different illumination angles. In this situation, different projections with opposite signs of $f(\theta,\varphi)$ will cancel each other during the averaging process in Fourier diffraction theorem over different illumination angles. For our numerical phantom, as we can calculate all of the 3×3 Jones matrix components, we can evaluate the accuracy of this approximation. In this regard, the xy component of the approximated scattering potential, V_{xy}^{appro}, and the true scattering potential, V_{xy}^{true}, as well as the 3D reconstruction of the second term in Eq. S28 are shown in Fig. S4. We calculated the mean squared error (MSE) for this approximation as 7%. Additionally, for a better comparison of the true scattering potential and the error, Figs. S4(e-f) show the histogram diagrams of these 3D reconstructions in the plane of best focus. According to these figures, most of the values for the error is concentrated on zero or near zero, while the true reconstruction is very well distributed.

4. RELATIONSHIP BETWEEN RECONSTRUCTIONS PERFORMED IN DIFFERENT POLARIZATION STATES

As discussed in the manuscript, the cross-polarized light shows zero intensities especially at the background regions, and it results in random phase values. This makes the calibration of the off-set phase (which is necessary due to the phase fluctuations in the holography setups), and unwrapping challenging. To overcome this issue, we use the idea to make the input and measured polarization states differ by 45°. So, we illuminate a sample with $+45^\circ$ and -45° polarization states (a and b) with respect to the XY coordinate, and measure X-polarized and Y-polarized lights. This configuration guaranties to have the background light intensity in all the measurements and avoid random phases. Now we explain how to convert these 4 tomographic reconstructions of the scattering potential, V_{xa}, V_{ya}, V_{xb}, and V_{yb} to the components of the scattering potential tensor, V_{xx}, V_{yx}, V_{xy}, and V_{yy}. At first, we find the relationship for the case with Born approximation. According to Eq. S12, for two experiments of illumination with a-polarized and b-polarized light, we have:

$$\overline{\overline{V}}(k_x-k_x^{in},k_y-k_y^{in},k_z-k_z^{in})=\frac{k_z}{2\pi j}\mathcal{F}_{2D}\left\{\begin{pmatrix}E^s_{xa}&E^s_{xb}\\E^s_{ya}&E^s_{yb}\end{pmatrix}\begin{pmatrix}\tilde{E}I_{xa}&\tilde{E}I_{xb}\\\tilde{E}I_{ya}&\tilde{E}I_{yb}\end{pmatrix}^{-1}\right\}(k_x,k_y) \tag{S29}$$

where $\tilde{E}I_{ij}$ is the amplitude of the input field component along i polarization when input field is $j=a,b$ polarized. Since, the input polarization is $\pm45^\circ$, we have $\tilde{E}I_{xa}=\tilde{E}I_{ya}=\tilde{E}I_{xb}=-\tilde{E}I_{yb}$. By rewriting Eq. S29,we can get:

$$\begin{aligned}\overline{\overline{V}}(k_x-k_x^{in},k_y-k_y^{in},k_z-k_z^{in})&=\frac{k_z}{2\pi j}\mathcal{F}_{2D}\left\{\frac{1}{2\tilde{E}I_{xa}}\begin{pmatrix}E^s_{xa}&E^s_{xb}\\E^s_{ya}&E^s_{yb}\end{pmatrix}\begin{pmatrix}1&1\\1&-1\end{pmatrix}\right\}(k_x,k_y)\\&=\frac{k_z}{2\pi j}\mathcal{F}_{2D}\left\{\frac{1}{2}\begin{pmatrix}E^s_{xa}/\tilde{E}I_{xa}+E^s_{xb}/\tilde{E}I_{xb}&E^s_{xa}/\tilde{E}I_{xa}-E^s_{xb}/\tilde{E}I_{xb}\\E^s_{ya}/\tilde{E}I_{ya}-E^s_{yb}/\tilde{E}I_{yb}&E^s_{ya}/\tilde{E}I_{ya}+E^s_{yb}/\tilde{E}I_{yb}\end{pmatrix}\right\}(k_x,k_y)\end{aligned} \tag{S30}$$

we can consider V_{ij}, $i\in x,y$, and $j\in a,b$, as the 3D scalar scattering potential which is reconstructed by applying the Wolf transform on $E^s_{ij}/\tilde{E}I_{ij}$. As a result, we will have:

$$\overline{\overline{V}}=\begin{pmatrix}V_{xx}&V_{xy}\\V_{yx}&V_{yy}\end{pmatrix}=\frac{1}{2}\begin{pmatrix}V_{xa}+V_{xb}&V_{xa}-V_{xb}\\V_{ya}-V_{yb}&V_{ya}+V_{yb}\end{pmatrix} \tag{S31}$$

In the case of the Rytov approximation, we can replace $E^s_{ij}/\tilde{E}I_{ij}$ with $\log(1+E^s_{ij}/\tilde{E}I_{ij})$ in Eq. S30. This gives us the same result as Eq. S31 to convert the reconstructed Rytov-based scalar scattering potentials to the elements of $\overline{\overline{V}}$.

As a result, based on the linear functionality of the scattering potential with scattered fields, achieved thanks to the single-scattering assumption, we can use Eq. S31 to calculate the scattering potential tensor elements using the $\pm45^\circ$-polarized data.

5. EFFECT OF A TILTED POLARIZER

According to the experimental setup in Fig. 3(a) of the manuscript, we put a polarizer after the imaging system to measure the desired output polarizer. However, this polarizer is illuminated obliquely while scanning the illumination angle. Therefore, the Jones matrix of a tilted polarizer changes depending on its angle and is different from when it is illuminated normally. To analyze the effect of tilted polarization, we use the Fainman-Shamir model [9]. According to this model which is for an ideal polarizer, the Jones matrix of a polarizer can be achieved as,

$$\overline{\overline{J}}_P=\frac{\left(\hat{P}_A-\hat{P}_A.\hat{k}_{in}\right)\left(\hat{P}_A-\hat{P}_A.\hat{k}_{in}\right)^\dagger}{1-\left(\hat{P}_A.\hat{k}_{in}\right)^2} \tag{S32}$$

in which, $\hat{P}_A$ is the unitary vector along which the polarizer/analyzer are aligned (in the plane of the polarizer), and $\hat{k}_{in}$ is the unitary vector of the incident wave-vector. In our setup we use

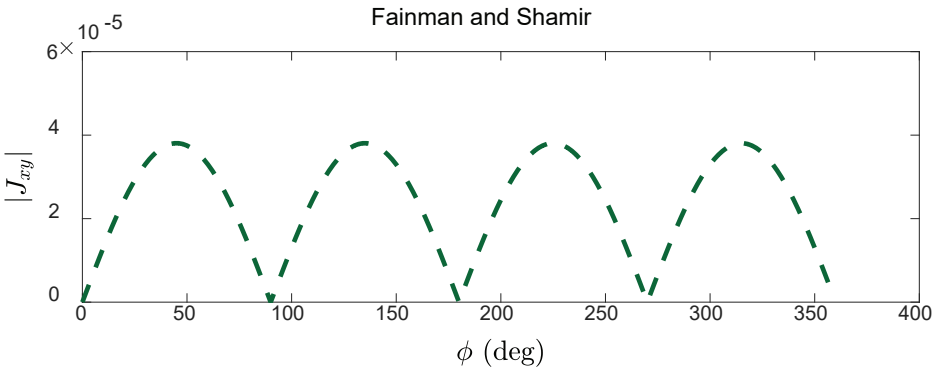

Fig. S5. The off-diagonal component of the Jones matrix of an ideal polarized as it is illuminated with a tilted beam as we scan φ.

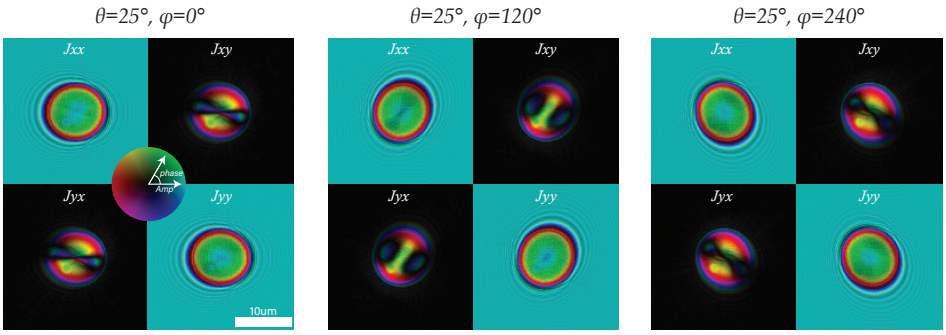

Fig. S6. The Jones matrix of the digital phantom calculated with the V-BPM for 3 different projections. Same data for 180 projections are used to reconstruct the 3D phantom.

a 60X imaging system which means a 60X angular demagnification. This way, the polarizer is illuminated with a 0.5° angle ($\sim 30°/60$). The off-diagonal term, J_{xy}, of the Jones matrix, J_P, is shown in Fig. S5. According to this figure, we can see that this term is very small, comparing to J_{xx} and we can completely neglect this effect. Specially, a calibration step, which measures both co and cross polarizations without the sample will handle these inaccuracies. Moreover, the most important issue to be considered for the tilted illumination is the rotational matrix described as Eq. (8) in the manuscript.

6. NUMERICAL RESULTS

Here, we present more figures about the numerical results partly presented in the manuscript. For the digital phantom which we discussed in the paper, we show the Jones matrix calculated for 3 different illumination angles, $\varphi = 0°$, $\varphi = 120°$, $\varphi = 240°$ in Fig. S6. Same as the paper, complex values are coded using the brightness and color (amplitude and phase, respectively) in the figure. The circular diffraction pattern along the illumination direction is clear in the amplitude of the total field. In the absence of the sample, the off-diagonal terms of the Jones matrix are zero, which means that there is no cross-polarization coupling. In Fig. S7, we show the full reconstruction of the refractive index tensor, which we showed only two of them, n_{xx}, and n_{yx} in Fig. 5 of the manuscript. For each component of the refractive index tensor, the first row shows the ground-truth and the second row shows the reconstruction using the polarization-sensitive ODT with Rytov approximation. Here, we show the YX, XZ, and YZ profiles of the 3D reconstruction.

An important issue regarding the refractive index tensor is the fact that the off-diagonal components of this tensor do not present any inherent information, by their own value, regarding the birefringence, or orientation of the slow-axis (or fast axis) of the sample. In fact, the latest

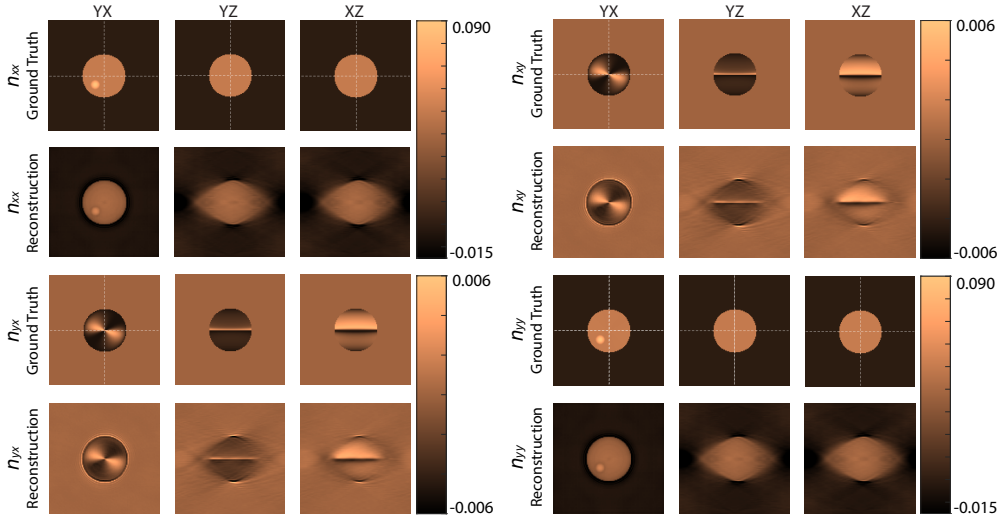

Fig. S7. Polarization-sensitive reconstruction of the digital phantom using the Rytov approximation. For each component of the tensor, we show the ground-truth and the reconstruction in YX, YZ and XZ planes. Dashed lines show the lines that we show the profile of the index along them.

parameters have a physical meaning about the anisotropy of the sample and the tensorial representation of the refractive index is the consequence of an unknown rotation of the sample with respect to its axis and the experiment coordinate system. It has been discussed in section 3.C of the manuscript that how the eigen-value characterization of the refractive index tensor can help to find some 3D parameters correlated with physical and inherent meanings. In fact, eigenvalues and eigen-vectors of a tensor are invariant under any unitary transformation such as coordinate rotation. In each voxel of the sample, the difference between the eigen-values of the 3D refractive index tensor can represent the birefringence of the sample and the orientation of the eigen-vector corresponding to the bigger (smaller) eigen-value can represent the direction of the slow-(fast-)axis of the sample. In Fig. S8 you can see the 3D birefringence and also the orientation of the slow-axis that are extracted from the eigen-value characterization of the refractive index tensor for the numerical phantom.

7. DENOISING AND ITERATIVE RECONSTRUCTION

Due to the coherent noise which exists in the holography technique, we used a denoising technique based on a 3D total-variation (TV) to a bit smooth-out our final reconstruction. In the denoising problem, we minimize the following cost function, to calculate the image $\hat{x}$ from the noisy image x:

$$\min_{\hat{x}} \left\{ \|\hat{x} - x\|^2 + \lambda R_{TV}(\hat{x}) \right\} \tag{S33}$$

in which, $R_{TV}(\hat{x})$ is the TV regularization and λ is the regularization parameter which determines how strongly this TV denoising regularization applies. However, a very important issue is that this denoising should not be confused with iterative techniques that are used to compensate the missing-cone problem. In the missing-information problem, on the other hand, we have an under-determined problem that we use total variation or a set of sparsity constraints to overcome. This has to be done using the minimization of such a cost function:

$$\min_{\hat{x}} \left\{ \|A\{\hat{x}\} - b\|^2 + \lambda R_{TV}(\hat{x}) \right\} \tag{S34}$$

for which A is some linear map which is usually the fourier transform in the case of missing-cone problem for ODT [10]. A more clear discussion on this topic is presented in a work by A. Beck and M. Teboulle [11] where they clarify the difference between the two problems of denoising and deblurring (which solves missing frequencies similar to the missing cone problem in ODT).

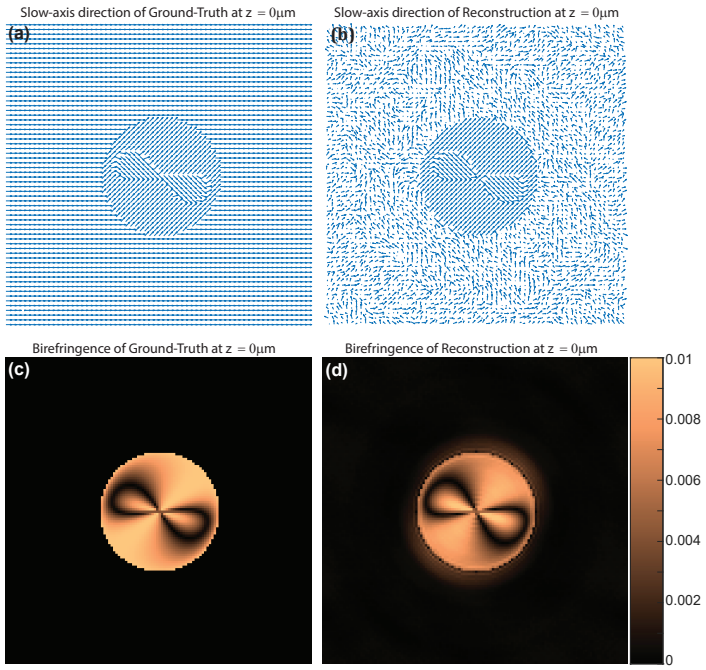

Fig. S8. Eigen-value characterization of the refractive index tensor of the digital phantom: (a) Profile of the 3D Slow-axis direction at $z = 0^{-}$m for the ground-truth, (b) Profile of the 3D Slow-axis direction at $z = 0^{-}$m for the 3D reconstruction, (c) Profile of the 3D Birefringence ($\mu_n^1 - \mu_n^2$) of the ground-truth, (d) Profile of the 3D Birefringence ($\mu_n^1 - \mu_n^2$) of the 3D reconstruction.

As a result, in our work we just used TV regularization to denoise the final reconstructions and we should not expect that the missing cone problem gets fixed. However, we also did an iterative reconstruction using TV regularization to solve the missing cone problem that we wish to extend in another work later. This method is based on the tensorial version of [10]. We use Eq. S34 where,

$$A\left\{\overline{\overline{V}}\right\} = \overline{\overline{V}}\left(k_x - k_x^{in}, k_y - k_y^{in}, k_z - k_z^{in}\right) \tag{S35a}$$

$$b = \frac{k_z^{in}}{2\pi j}\mathcal{F}_{2D}\left\{\begin{pmatrix} E_{x1}^s & E_{x2}^s \\ E_{y1}^s & E_{y2}^s \end{pmatrix}\begin{pmatrix} E_{x1}^i & E_{x2}^i \\ E_{y1}^i & E_{y2}^i \end{pmatrix}^{-1}\right\} \tag{S35b}$$

with the parameters similar to what is defined in the manuscript. The iterative reconstruction is presented in Fig. S9. In the first row we show the ground-truth, in the second row we show the direct Rytov-based reconstructions as presented in the main paper, and in the third row, we show the iterative reconstruction using TV regularization. As is clear from this figure, the third-row reconstructions do not include any elongation along z-axis in contrast to the second row. This shows that similar to the sclar ODT, iterative techniques with a linear forward model, or even nonlinear forward model can be used for polarization-sensitive ODT.

8. MUSCLE TISSUE EXPERIMENT

To show the importance of the PS-ODT for biological samples, we did the experiment for a muscle tissue. Muscle tissue is birefringent due to its fibrous structures and A-bands (thick filaments) inside the sarcomere of the muscle fiber. The fresh frozen muscle section is embedded in cryo medium and cut with $20\mu m$ thickness. This thickness is enough to get a nice and strong cross-polarized light and at the same time keep the single-scattering condition satisfied. In Fig. S10, we present the cross-polarized light (U_{xy}^s) intensity. In Fig. S11, the extracted holographical phase of one of the projections is shown for the muscle tissue. In Fig. S11(a), the phase of the

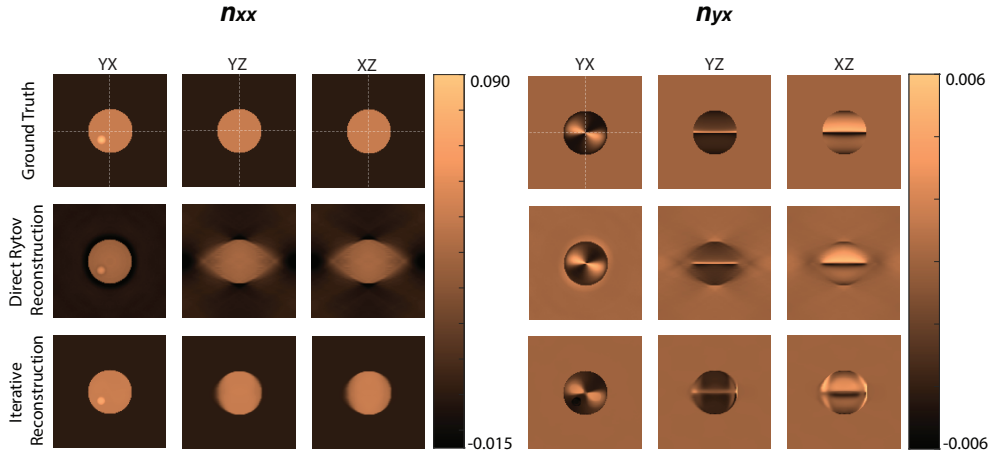

Fig. S9. Iterative reconstruction of the digital phantom: 1st row: ground-truth, 2nd row: direct iterative reconstructions, 3rd row: iterative reconstruction using TV regularization.

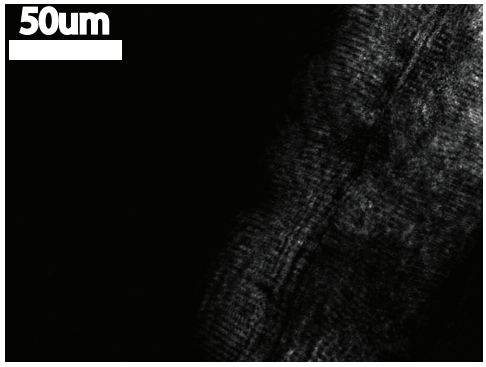

Fig. S10. The cross-polarized light amplitude $|U^s_{xy}|^2$ which is measured for the muscle tissue.

cross-polarized light is presented (U^s_{xy}) while in Fig. S11(b) we show the phase of (U^s_{xa}). In Fig. S11(a), due to the zero background intensity, the background phase is random which makes the calibration (because of the ambiguity of the phase of the reference beam) and phase unwrapping difficult. On the other hand, using 45° polarization idea, the background phase of the complex field (U^s_{xa}) is nice, since the input and output polarizations have only 45° of miss-alignment and as a result we have a background intensity. This helps to unwrap and calibrate the phase of the complex fields easily and then convert the reconstructions to the XY coordinate system.

REFERENCES

1. A. Ishimaru, *Wave propagation and scattering in random media*, vol. 2 (Academic press New York, 1978).
2. A. Ciattoni, P. Di Porto, B. Crosignani, and A. Yariv, "Vectorial nonparaxial propagation equation in the presence of a tensorial refractive-index perturbation," JOSA B **17**, 809–819 (2000).
3. Z. Tong and O. Korotkova, "Theory of weak scattering of stochastic electromagnetic fields from deterministic and random media," Phys. Rev. A **82**, 033836 (2010).
4. E. Wolf, "Three-dimensional structure determination of semi-transparent objects from holographic data," Opt. communications **1**, 153–156 (1969).
5. R. Gilmore, "Baker-campbell-hausdorff formulas," J. Math. Phys. **15**, 2090–2092 (1974).
6. M. Feit and J. Fleck, "Beam nonparaxiality, filament formation, and beam breakup in the self-focusing of optical beams," JOSA B **5**, 633–640 (1988).

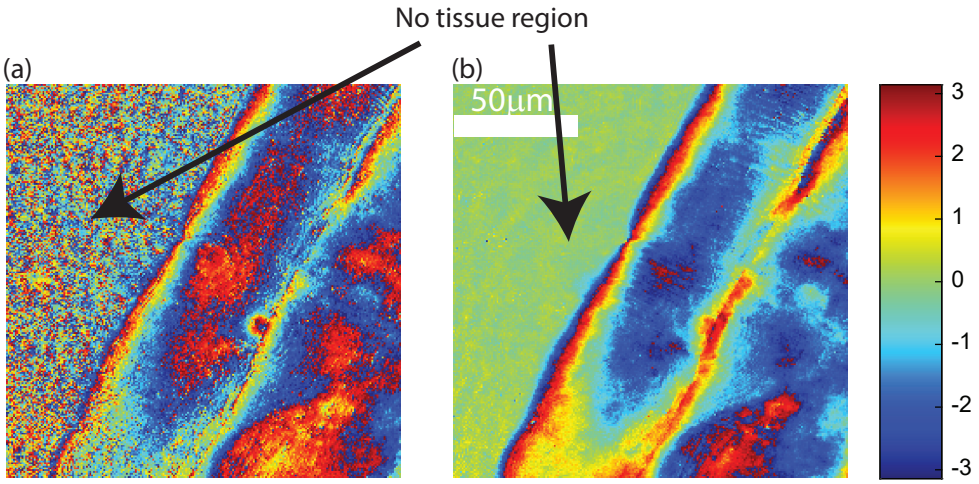

Fig. S11. The phase of the scattered field. (a) for U^s_{xy} and (b) for U^s_{xa}. The background phase is random due to the zero intensity in the cross-polarized light. By contrast, in (b) the background phase can be easily calibrated and unwrapped.

7. C. D. Meyer, *Matrix analysis and applied linear algebra*, vol. 71 (Siam, 2000).
8. Y. Bao and T. K. Gaylord, "Clarification and unification of the obliquity factor in diffraction and scattering theories: discussion," JOSA A **34**, 1738–1745 (2017).
9. Y. Fainman and J. Shamir, "Polarization of nonplanar wave fronts," Appl. optics **23**, 3188–3195 (1984).
10. J. Lim, K. Lee, K. H. Jin, S. Shin, S. Lee, Y. Park, and J. C. Ye, "Comparative study of iterative reconstruction algorithms for missing cone problems in optical diffraction tomography," Opt. express **23**, 16933–16948 (2015).
11. A. Beck and M. Teboulle, "Fast gradient-based algorithms for constrained total variation image denoising and deblurring problems," IEEE transactions on image processing **18**, 2419–2434 (2009).